Crystal growth, crystal field evaluation and spectroscopy for thulium in monoclinic $KGd(WO_4)_2$ and $KLu(WO_4)_2$ laser crystals

2008 J. Phys.: Condens. Matter 20 345219

(http://iopscience.iop.org/0953-8984/20/34/345219)

J. Phys.: Condens. Matter **20** (2008) 345219 (9pp) doi:10.1088/0953-8984/20/34/345219

Crystal growth, crystal field evaluation and spectroscopy for thulium in monoclinic $KGd(WO_4)_2$ and $KLu(WO_4)_2$ laser crystals

M C Pujol[1], C Cascales[2], M Aguiló[1] and F Díaz[1]

[1] Física i Cristal.lografia de Materials (FiCMA), Universitat Rovira i Virgili (URV), Campus Sescelades c/ Marcel.lí Domingo, s/n, E-43007 Tarragona, Spain
[2] Instituto de Ciencia de Materiales de Madrid ICMM, Consejo Superior de Investigaciones Científicas CSIC, E-28049 Cantoblanco, Madrid, Spain

E-mail: ccascales@icmm.csic.es

Received 26 February 2008, in final form 26 June 2008
Published 6 August 2008
Online at stacks.iop.org/JPhysCM/20/345219

Abstract

A comparison of the suitability of two Tm^{3+}-doped monoclinic double tungstate $KRE(WO_4)_2$ ($RE = Gd^{3+}$ or Lu^{3+}) laser crystals was carried out based on crystal growth conditions and the strength of crystal field interactions provided by the corresponding host at the Tm^{3+} site. For the same 3% Tm^{3+} substitution level, macrodefect-free single crystals can be grown, with higher cooling rates and lower temperatures for the $KLu(WO_4)_2$ host. Furthermore, the information provided by the phenomenological crystal field analysis of low temperature polarized spectroscopic data for both hosts indicates that $KLu(WO_4)_2$ exhibits the stronger crystal field and thus an enhanced $^3H_6$ splitting compared to $KGd(WO_4)_2$. Considering these factors as well as its calculated higher emission cross sections, it is concluded that $KLu(WO_4)_2$ is the most suitable of the two hosts for Tm^{3+} doping.

S Supplementary data are available from stacks.iop.org/JPhysCM/20/345219

(Some figures in this article are in colour only in the electronic version)

1. Introduction

Laser operation near 2 μm has wide applications related to its eye-safe nature in medicine [1] and atmospheric sensing [2, 3]. Although traditionally solid-state lasers for this spectral range were based on Ho^{3+}-doped crystals, new pumping technologies using commercially available high power AlGaAs diode lasers are promoting their replacement for suitable Tm^{3+}-doped crystals operating on the $^3F_4 \rightarrow {}^3H_6$ emission transition. The high absorption of Tm^{3+} at 800 nm makes possible an efficient direct pumping of its $^3H_6 \rightarrow {}^3H_4$ transition by the above diode lasers. The vibrational interaction of Tm^{3+} with the crystal host leads to absorption and emission bands broader than those of Ho^{3+}, which is strongly shielded from host interactions. Absorption bandwidth broadening supposes better overlap with the pump source and some reduction in the sensitivity to thermal drifts of the pump wavelength, while broader emission lines are an advantage for tunable and ultrashort pulse laser operation [4]. Moreover, since the $^3F_4$ population is achieved through cross-relaxation between an ion in the ground $^3H_6$ state and an excited ion in the $^3H_4$ state [5], the expected quantum defect of laser emission around 2 μm will be reduced in Tm^{3+}-doped crystals.

Efficient 2 μm Tm^{3+} continuous wave laser operation has been demonstrated with different well-known laser hosts, such as YAG [2, 6], YVO_4 [7] and in the monoclinic potassium-based double tungstates of formula $KRE(WO_4)_2$, RE being a trivalent transparent rare earth. In the last family of crystals, hereafter referred to as KREW, laser oscillation in the 2 μm range has been obtained for a Ti–sapphire pumped Tm^{3+}–KGdW crystal, which shows large tunability from 1790 to

2042 nm, and a slope efficiency of 40% [8]. Beneficial effects on laser slope efficiency [9] while keeping similar thermo-optical properties [10] have been claimed in replacing Gd^{3+} with Lu^{3+} in crystalline hosts. Following this emerging trend, ≈2 μm Tm^{3+} laser emission was demonstrated in the KLuW crystal, with both Ti–sapphire and AlGaAs diode pumping, this last configuration yielding a higher slope efficiency, 69%, and a output power of 4 W, although with a somewhat reduced tuning range, 1800–1987 nm [11, 12].

The main disadvantage of Tm^{3+} as a quasi-three-level laser system for the $^3F_4 \rightarrow {}^3H_6$ transition is the thermal population of the terminal level, which belongs to the ground state multiplet. Consequently, the laser performance depends critically on the operational temperature and host-related properties, such as the crystal field (CF) strength, which has to be large enough to achieve the desirable extended $^3H_6$ splitting. Previous studies on low temperature spectroscopic properties of Tm^{3+} in both KGdW [13] and KLuW [14] hosts reveal some inconsistencies in the established sequences of energy levels. For example, the unexpectedly large differences in the 13 observed energy levels for the $^3H_6$ ground state, considering the similarity between the hosts [13, 14]. These results illustrate the difficulties in the determination of the correct energy level sequence for Tm^{3+} solely from experimental spectroscopic data, even at cryogenic temperatures, given the uncertainty in the determination of the number of bands and their polarization nature. In fact, observed spectroscopic data must be supported by consistent and accurate modeling of CF interactions in order to establish the correct $4f^{12}$ Tm^{3+} configuration in a given crystal host [4, 15]. Often, disregarding such CF analysis can lead to errors in the evaluation of the spectroscopic parameters involved in laser operation, such as the $^3F_4$ and $^3H_6$ partition functions.

In this work we compare KGdW and KLuW hosts for Tm^{3+} doping, first testing for the most favorable conditions for the crystal growth using the top-seeded solution growth–slow cooling technique (TSSG-SC). Then, the position and irreducible representations (IR) of observed Tm^{3+} Stark levels of KGdW and KLuW hosts will be established from the CF analysis of measured optical spectra recorded in the 6–300 K temperature range. The least-squares fit of observed energy level schemes and the calculated ones derived through a phenomenological model using an effective Hamiltonian, which simultaneously includes free-ion and crystal field interactions, will allow us to derive the best fitted set of CF parameters for each host, and thus extract reliable information to compare the Tm^{3+} splittings and to calculate the partition functions of levels involved in 2 μm laser operation, that is, $^3F_4$ and $^3H_6$, in both KGdW and KLuW laser hosts.

2. Experimental crystal growth procedures and details

Crystal growth of Tm-KGdW and Tm-KLuW by the TSSG-SC using a $K_2W_2O_7$ solvent has been previously reported [14, 16]. Because both KREW compounds have a polymorphic transition below their melting point, crystal growth is not possible directly from the liquid phase, so a high temperature solution growth method was required. Experiments with a 3% Tm^{3+} doping level have been performed under similar conditions in order to compare the growth processes of Tm-KGdW and Tm-KLuW. In each case, the composition of the solution was 11.5/88.5 solute/solvent molar ratio. The precursor oxides were K_2CO_3 (Fluka, 99.0%), Gd_2O_3 (Aldrich, 99.9%), Lu_2O_3 (Aldrich, 99.9%), Tm_2O_3 (Aldrich, 99.9%) and WO_3 (Fluka, 99.9%). A platinum crucible was placed in a vertical furnace in such a way that the axial temperature gradient in the solution was about 1.3 K cm^{-1} (from the hot bottom), while the radial temperature gradient was about 1 K cm^{-1} (hot crucible wall). After the solution had been homogenized, the saturation temperature, T_s, was determined with a KREW *b*-oriented seed in contact with the free surface of the solution. Then, a constant rotation of 40 rpm was applied to the crystal and a 0.1 K h^{-1} cooling rate was used to create a supersaturated solution, which drives the crystal growth. Electron probe microanalysis–wavelength dispersive spectrometer (EPMA-WDS) results for the Tm^{3+} concentration in the crystals were obtained using a Cameca Camebax SX 50.

Polarized optical absorption measurements were performed at room temperature and at 6 K using a Cary Varian 500 spectrophotometer, with a resolution of 0.025 nm in the UV–vis region and 0.2 nm in the NIR region, as described in [13, 14]. In the low temperature experiments performed at 6 K, an Oxford Instruments cryostat (SU 12 model) with helium-gas closed-cycle flow was used. The samples were parallelepipeds with their faces oriented parallel to a principal optical plane.

3. Theoretical background for the modeling of crystal field interactions

The method used for calculating the energy levels of the Tm^{3+} in its crystalline environment is based on the central-field approximation. In this analysis, the free-ion (FI) and CF interactions have been simultaneously considered when fitting the observed energy levels. In this manner, all intermediate coupling and CF J-mixing effects are included in the calculations, and arbitrary adjustments of the barycenter of the multiplets have been avoided. The FI Hamiltonian is parameterized as [17]

$$H_{\mathrm{FI}} = H_0 + \sum_{k=0,1,2,3} E_k \mathrm{e}^k + \zeta_{4\mathrm{f}} A_{\mathrm{SO}} + \alpha L(L+1) + \beta G(G_2) + \gamma G(R_7) + \sum_{k=0,2,4} M^k m_k + \sum_{i=2,4,6} P^i p_i \quad (1)$$

where H_0 corresponds to the spherically symmetric one-electron term of the Hamiltonian. The principal terms in the Hamiltonian are the Racah parameters, E_k, and the spin–orbit coupling constant, ζ_{4f}, which represent the electrostatic interaction between equivalent f electrons and the coupling of the electron spin with the orbital momentum, respectively. The Trees parameters, α, β and γ, account for the two-body interactions. Although they correspond to smaller interactions, the remaining terms play an important role in the accurate description of the energy level structure of Tm^{3+}:

Table 1. Crystal growth parameters of 3% at Tm-KRE$(WO_4)_2$, RE = Gd or Lu, single crystals. (Note: A: temperature gradient in the solution (K mm^{-1}). B: $Tm_2O_3/(RE_2O_3 + Tm_2O_3)$ ratio in the solution (at.%). C: seed orientation. D: cooling rate (K h^{-1}). E: cooling interval (K). F: crystal weight, (g). G: growth rate ($(\times 10^{-4})$, g h^{-1}). H: macrodefects. I: crystal dimensions along the *c* direction (mm). J: crystal dimensions along the a^* direction (mm). K: crystal dimensions along the *b* direction (mm). L: saturation temperature (K).)

Host	A	B	C	D	E	F	G	H	I	J	K	L
KLuW	0.13	3	*b*	0.1	20	5.8810	294	None	14.27	9.3	12.9	1178.8
KLuW	0.13	3	*b*	0.1	20	5.6229	281	None	11.32	9.28	7.15	1179.1
KGdW	0.123	3	*b*	0.1	20	5.9388	297	Some cracks	16.8	6.31	12.22	1182.3
KGdW	0.123	3	*b*	0.1	17.1	5.1258	297	Some cracks and inclusions	16.1	6.2	12.4	1183.1

the magnetically correlated corrections such as spin–spin and spin–other-orbit interactions, which can be simulated through the M^k parameters, also called Marvin integrals, and the electrostatically correlated spin–orbit interactions described by the P^i integrals.

The one-electron CF Hamiltonian is given in the formalism of Wybourne [18] by

$$H_{\mathrm{CF}} = \sum_{i=0}^{N} \sum_{k=0}^{\infty} \sum_{q=-k}^{k} B_q^k C_q^k(i) \tag{2}$$

where $C_q^k(i)$ is a spherical tensor of rank k, with components $q \cdot B_q^k$ are the CF parameters. N is the number of electrons and i represent the ith electron. For f electrons $k \leqslant 6$. The expansion of the CF Hamiltonian is symmetry-dependent. For the C_2 symmetry of Tm^{3+} in KGdW and KLuW hosts, the H_{CF} is expanded as

$$\begin{aligned} H_{C_2}^{\mathrm{even}} &= B_0^2 C_0^2 + B_2^2(C_{-2}^2 + C_2^2) + i B_2^2(C_{-2}^2 - C_2^2) \\ &+ B_0^4 C_0^4 + B_2^4(C_{-2}^4 + C_2^4) + i B_2^4(C_{-2}^4 - C_2^4) \\ &+ B_4^4(C_{-4}^4 + C_4^4) + i B_4^4(C_{-4}^4 - C_4^4) \\ &+ B_0^6 C_0^6 + B_2^6(C_{-2}^6 + C_2^6) + i B_2^6(C_{-2}^6 - C_2^6) \\ &+ B_4^6(C_{-4}^6 + C_4^6) + i B_4^6(C_{-4}^4 - C_4^6) \\ &+ B_6^6(C_{-6}^6 + C_6^6) + i B_6^6(C_{-6}^6 - C_4^6). \end{aligned} \tag{3}$$

Only the even terms have to be considered for the splitting of the levels under the crystal field because the odd parts are zero within one configuration. The above 15 CF parameters (9 real B_q^k and 6 complex $i B_q^k$) have been reduced to 14 by a proper choice of the reference axis system, which cancels the complex $i B_2^2$ parameter. The correct procedure for the simulation of the energy level scheme of Tm^{3+} involves the simultaneous treatment of both the FI and CF effects using the untruncated basis set of wavefunctions. The best fit of parameters was obtained, in each case, by the least-squares refinement between the observed and calculated energy level values through a minimization of the root-mean-square (rms) function $\sigma = [\Sigma(\Delta_i)^2/(L-p)]^{1/2}$, where Δ_i is the difference between observed and calculated energies, L is the number of levels and p is the number of parameters freely varied. The IMAGE routine was used to perform the CF analysis and adjustment of observed energy levels [19–21].

As useful tools to measure the CF interaction strength, mainly in order to establish quantitative comparisons between both KGdW and KLuW hosts, or within the same host for different $4f^N$ configurations, the relative S^k ($k = 2, 4, 6$) and total S^T CF strength parameters have also been calculated with the formalism of Chang *et al* [22]:

$$S^k = \left\{ 1/(2k+1) \left[(B_0^k)^2 + 2 \sum_q \left[(B_q^k)^2 + (i B_q^k)^2 \right] \right] \right\}^{1/2}$$
$$S^T = \left[\tfrac{1}{3} \sum_k S^{k^2} \right]^{1/2}. \tag{4}$$

4. Experimental results

4.1. Crystalline structure and crystal growth

Both Tm-KREW (RE = Gd, Lu) crystals belong to the monoclinic system, with space group $C2/c$ (No 15) and unit cell parameters $a = 10.652(4)$ Å, $b = 10.374(5)$ Å, $c = 7.582(2)$ Å, $\beta = 130.80(2)^\circ$ for KGdW [23], and $a = 10.576(7)$ Å, $b = 10.214(7)$ Å, $c = 7.487(2)$ Å, $\beta = 130.68(4)^\circ$ for KLuW [24]. The RE is coordinated with 8 oxygen atoms, which form a distorted square antiprism with four different RE–O distances. The local symmetry of RE in its first coordination sphere only contains a C_2 axis parallel to the *b* axis of the lattice.

For the above crystals, the principal axes of the optical indicatrix (i.e. the geometric figure that shows the index of refraction and vibration direction for light passing in any direction through this biaxial material) have previously been determined [23, 24]. In each case, the axis with lowest refractive index is labeled N_p and is parallel to the crystallographic *b* axis. The principal axis with the highest refractive index is labeled N_g and is in the *ac* plane forming an angle ∼20° with the *c* axis in the clockwise direction when looking from the positive end of the *b* axis. Finally, the principal axis with intermediate refractive index is labeled N_m and is in the *ac* plane orthogonal with the N_g principal axis.

Table 1 summarizes the different parameters of crystal growth for the 3% at Tm-KGdW and 3% at Tm-KLuW. The crystal growth temperatures for KGdW are always higher than for KLuW in the $K_2W_2O_7$ solvent. This fact is supported by the solubility curve of undoped KGdW [23] and undoped KLuW [25] in the $K_2W_2O_7$ solvent, in which the temperature of growth for 11.5% molar solute in solution is around 1186 and 1149 K, respectively. Also, the Tm^{3+} doping decreases the saturation temperature for KGdW, while increasing it for KLuW. The average growth rate in KGdW is slightly higher than KLuW, which can be attributed to its slightly higher

Table 2. Summary of the EPMA results for 3% at $KRE_{1-x}Tm_x(WO_4)_2$, RE = Gd or Lu.

	x	Distribution coefficient, K	$[Tm^{3+}]$ (10^{19} cm^{-3})	Stoichiometric formula
3 at.% Tm-KGdW	2.45	0.82	15.4	$KGd_{0.975}Tm_{0.025}(WO_4)_2$
3 at.% Tm-KLuW	3.70	1.23	2.41	$KLu_{0.963}Tm_{0.037}(WO_4)_2$

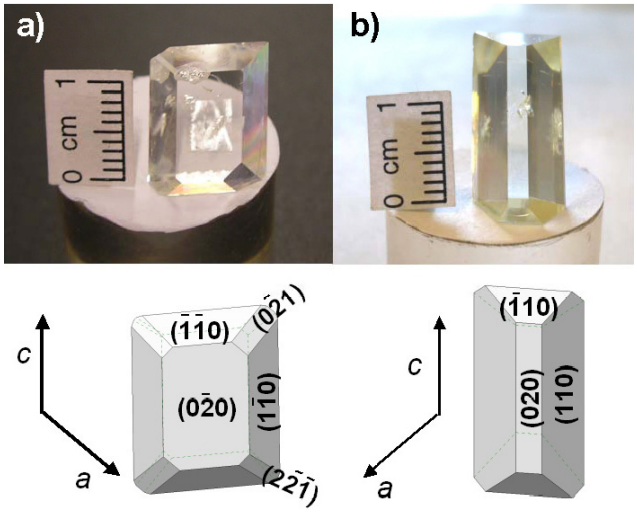

Figure 1. Photographs of Tm-KREW TSSG grown crystals and their morphological schemes. (a) Tm-KGdW; (b) Tm-KLuW.

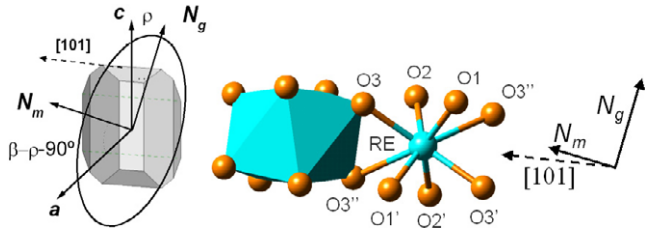

Figure 2. REO_8 coordination polyhedron in the monoclinic structure of KREW crystals, RE = Gd, Lu. It consists in a distorted square antiprism with C_2 symmetry. The REO_8 chain is running along the [101] direction. This crystallographic direction is located at 17.09° and 14.27° anticlockwise, for KGdW and KLuW, respectively from the principal axis N_m with positive b axis pointing to the observer. In the right, a crystal habit of KREW crystals, and the principal optical frame, N_g, N_m and N_p. The angle between N_g and the c crystallographic direction, ρ, is 21.5° and 18.5° for KGdW and KLuW, respectively.

growth temperature, leading to a lower solution viscosity, as expected.

Transparent single crystals of both compounds were obtained, but Tm-KGdW crystals showed some macrodefects. Lower cooling rates are needed to obtain macrodefect-free single crystals of Tm-KGdW. So, as in [26], the cooling rate for Tm-KGdW growth without macrodefects must be lowered to about 0.025 °C h^{-1}.[3]

Both Tm-KGdW and Tm-KLuW crystals have the same crystallographic faces, but with small morphological changes. The Tm-KLuW crystal is longer along the b direction, that is, it is bulkier in comparison with KGdW, whose crystal habit is more tabular. This is related to the higher growth velocity of the (010) face in KLuW crystals. Figure 1 shows a photograph of the crystals along with their morphological schemes. Introduction of doping ions to KLuW did not result in the appearance of new faces in the habit of the crystal.

The distribution coefficients of Tm^{3+} ion substituting Gd^{3+} and Lu^{3+} ions in KGdW and KLuW are defined as the ratio between the molar concentration in the corresponding KREW crystal and in the growth solution:

$$K_{Tm^{3+}} = \frac{(\text{moles } Tm^{3+}/(\text{moles } Tm^{3+} + \text{moles } RE^{3+}))_{\text{crystal}}}{(\text{moles } Tm^{3+}/(\text{moles } Tm^{3+} + \text{moles } RE^{3+}))_{\text{solution}}}. \quad (5)$$

[3] Usually higher growth rates allow obtaining larger crystals maintaining higher cooling rates. Therefore, with high growth rates it is sometimes necessary to reduce the supersaturation in the solution in order to avoid a fast growth, generating macrodefects. Consequently, to grow macrodefect-free Tm-KGdW crystals, the cooling rates must be decreased as in [26], just motivated by their faster growth rate.

For the constituent elements K, W, RE and O, undoped KREW was used as the standard reference. Table 2 resumes EPMA results. Under the same crystal growth conditions, Tm^{3+} shows a higher distribution coefficient in KLuW than in KGdW, which is expected taking into account the ionic radii of Tm^{3+} and the substituted cation in each host, 0.994, 1.053 and 0.977 Å, for Tm^{3+}, Gd^{3+} and Lu^{3+}, respectively. Also, the Tm^{3+} distribution coefficient in KGdW reported here is lower than previously reported [16]. This could indicate that lower cooling rates favor the introduction of Tm^{3+} in the growth of the Tm-KGdW crystal.

4.2. Interpretation of low temperature spectroscopic data, irreducible representation assignment and simulation of Tm^{3+} energy level schemes

The $4f^{12}$ ground state configuration of Tm^{3+} consists of 13 $^{2S+1}L_J$ free-ion manifolds extending from the ground state $^3H_6$ up to the singlet level $^1S_0$ at ∼75 000 cm^{-1}. The transparency windows of KGdW and KLuW single crystals have a cutoff wavelength at the UV band edge, around 320 nm (31250 cm^{-1}) [12, 16] and thus the 8 levels situated below this threshold, $^3H_6$, $^3F_4$, $^3H_5$, $^3H_4$, $^3F_3$, $^3F_2$, $^1G_4$ and $^3P_2$, are accessible by standard optical absorption and photoluminescence spectroscopy [12–14].

For the C_2 point site symmetry of Tm^{3+} substituting Gd^{3+} or Lu^{3+} in KGdW and KLuW crystals (figure 2), the electrostatic CF effect lifts the $(2J + 1)$ degeneracy of free-ion levels, which are split into 91 Stark levels characterized by irreducible one-dimensional representations (IR) labeled Γ_1 and Γ_2 according to the notation of Koster [27]. The number of these levels and the corresponding IR for each J value are

listed as: $J = 0$, Γ_1; $J = 1$, $\Gamma_1 + 2\Gamma_2$; $J = 2$, $3\Gamma_1 + 2\Gamma_2$; $J = 3$, $3\Gamma_1 + 4\Gamma_2$; $J = 4$, $5\Gamma_1 + 4\Gamma_2$; $J = 5$, $5\Gamma_1 + 6\Gamma_2$, and $J = 6$, $7\Gamma_1 + 6\Gamma_2$.

Since the principal optical N_p axis of the crystals coincides with the twofold C_2 axis of the RE point site (which is aligned with the crystallographic b axis), spectra obtained with light polarized along the N_p axis (those labeled p) correspond to the z polarization in the group theory. Furthermore, the principal optical axes N_g and N_m are in the ac plane, with N_m orthogonal to N_g. In this way, selection rules for induced electric dipole (ED) transitions must be interpreted as $\Gamma_1 \rightarrow \Gamma_1$ (p polarization), $\Gamma_1 \leftrightarrow \Gamma_2$ (m, g polarizations) and $\Gamma_2 \rightarrow \Gamma_2$ (p polarization) [28]. Furthermore, some transitions can possess a non-negligible magnetic dipole (MD) character, like $^3H_5 \leftrightarrow {}^3H_6$ (see table 1 of [29]). The selection rules are, in this case, $\Gamma_1 \rightarrow \Gamma_1$ (R_p polarization), $\Gamma_1 \leftrightarrow \Gamma_2$ (R_m, R_g polarizations) and $\Gamma_2 \rightarrow \Gamma_2$ (R_p polarization). It must be noted that the intensity changes of the OA measured parallel to the N_m and N_g principal axes sometimes are much larger than those predicted by the refractive index dependence of the oscillator strengths. However, as a first approximation we will consider them to be equivalent.

In both KGdW and KLuW crystals, the position of the fundamental absorption band precludes the observation of $^3P_0 \sim 35\,000$ cm^{-1}, which is the other non-degenerate state for Tm^{3+} $4f^{12}$ apart from $^1S_0$. Hence, ascertaining the IR of the $^3H_6$ ground state Stark level through the observation of the polarization of the optical transitions is not a direct process. To proceed with the CF analysis we have first simulated the sequence of Tm^{3+} energy levels in KGdW using a set of 'smoothed' CF parameters that we derive from the earlier analysis of the Pr^{3+} [30], Ho^{3+} and Er^{3+} [31] configurations in the same KGdW host, using Tm^{3+} FI parameters from a previous study [15].

In this calculation the Tm^{3+} $4f^{12}$ C_2 energy levels are distributed in two submatrices, according to the values of the crystal quantum numbers $\mu = 0$ and 1 [18]. For the C_2 point symmetry each submatrix is associated with only one IR, Γ_1 or Γ_2, which make the polarization assignments easier. These calculated matrices contain 49 and 42 Stark energy levels, and since the first one includes $^3P_0$ and $^1S_0$ levels, it must correspond to IR Γ_1. With this information, we determine that the IR assignment of observed Stark levels for Tm-doped KGdW is consistent with IR Γ_2 for $^3H_6(0)$. The analogous energy levels derived from calculations with CF parameters obtained from the semi-empirical Simple Overlap Model CF model [32–34], using the measured crystallographic positions of the first coordination sphere of ligands around Tm^{3+} in KGdW [35], fully agree with the above preliminary phenomenological approach. Furthermore, these initial simulations allow us to identify two important facts: first, the energy difference between $^3H_6(0)$ and the first excited $^3H_6(1)$ level should be very small (~1–2 cm^{-1}), with equal thermal populations at low temperatures, according to the Boltzmann distribution; and secondly, each of these levels appears in a submatrix, i.e. they belong to different IR, Γ_2 and Γ_1, respectively. These facts qualitatively explain that some transitions are simultaneously seen in p, and m or g polarizations, since contributions from $^3H_6(0)$ and $^3H_6(1)$, although observed as sharp peaks, cannot be completely resolved, appearing thus as only slightly shifted or even overlapped peaks. Figure 3 shows the low temperature optical absorption of the $^3F_4$ and $^3H_4$ levels for Tm^{3+} in KGdW and KLuW.

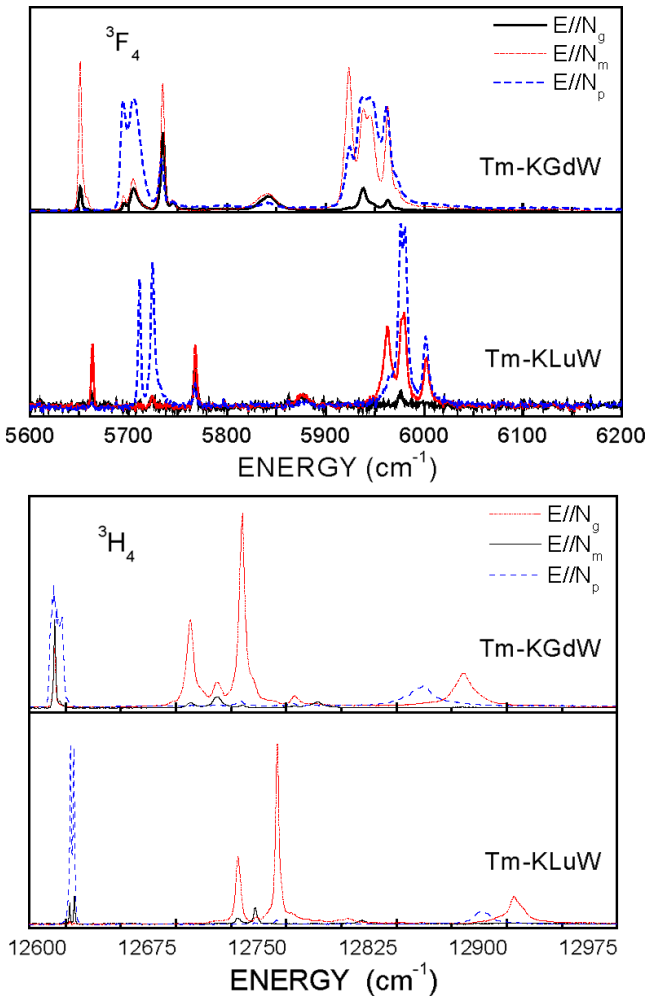

Figure 3. 6 K optical absorption spectra for the $^3H_6 \rightarrow {}^3F_4$ and $^3H_6 \rightarrow {}^3H_4$ transitions for Tm-KGdW and Tm-KLuW.

From the low temperature OA and PL spectra an energy level scheme of 51 CF Stark levels for Tm^{3+} in KGdW has been derived. These energy levels, for which the main component is indicated in each case, have been labeled Γ_1 or Γ_2, see table 3. Files containing all components of the associated wavefunction with contributions greater than 10^{-5} for each Stark level of Tm^{3+} in both KGdW and KLuW crystals are available as supplementary material (available at stacks.iop.org/JPhysCM/20/345219).

The sparse number of observed CF levels is not unusual for the Tm^{3+} $4f^{12}$ configuration in structurally ordered hosts, 27 in Tm-$LaCl_3$ [36], 56 in Tm-LaF_3 [17], 45 for Tm-$LiYF_4$ [37], 55 in Tm-GdOCl [38], 32 in Tm-K_2YF_5 [39], 42 in Tm, Ho-BaY_2F_8, [40], 52 in Tm-$BiYGeO_5$, [15] and it is even more reduced when disordered matrices, such as the tetragonal double tungstate laser crystal Tm-$NaLu(WO_4)_2$ [4] or molybdate $NaLa(MoO_4)_2$, [41] are considered.

Table 3. 6 K observed (E_o)[a] and calculated (E_c) energy levels (cm^{-1}) of Tm^{3+} in $KRE(WO_4)_2$, RE = Gd^{3+} or Lu^{3+}, single crystals. IR indicates the irreducible representation of the energy level. (Note: polarized optical absorption spectra have resolutions of 0.025 nm in the UV–vis region and 0.2 nm in the NIR region, see [13, 14]. Calculated Stark levels have the precision imposed by errors in free-ion and CF parameters derived from phenomenological fits, see table 4.)

$KGd(WO_4)_2$								$KLu(WO_4)_2$							
Main component	IR	E_o	E_c	Main component	IR	E_o	E_c	Main component	IR	E_o	E_c	Main component	IR	E_o	E_c
$^3H_6$	$_1\Gamma_2$	0	0	$^3H_4$	$_1\Gamma_2$	—	12 676	$^3H_6$	$_1\Gamma_2$	0	−3	$^3H_4$	$_0\Gamma_1$	12 717	12 717
	$_0\Gamma_1$	—	−2		$_0\Gamma_1$	12 685	12 676		$_0\Gamma_1$	—	−4		$_1\Gamma_2$	12 729	12 722
	$_2\Gamma_1$	104	105		$_4\Gamma_1$	—	12 724		$_2\Gamma_1$	135	140		$_4\Gamma_1$	12 744	12 739
	$_1\Gamma_2$	127	119		$_4\Gamma_1$	—	12 803		$_1\Gamma_2$	155	149		$_4\Gamma_1$	12 790	12 816
	$_6\Gamma_1$	193	190		$_3\Gamma_2$	12 843	12 842		$_6\Gamma_1$	224	221		$_{-3}\Gamma_2$	—	12 835
	$_6\Gamma_1$	223	228		$_{-3}\Gamma_2$	—	12 859		$_6\Gamma_1$	256	262		$_3\Gamma_2$	12 883	12 903
	$_3\Gamma_2$	250	249		$_2\Gamma_1$	12 871	12 876		$_3\Gamma_2$	279	284		$_2\Gamma_1$	12 906	12 908
	$_2\Gamma_1$	300	303						$_2\Gamma_1$	346	353				
	$_5\Gamma_2$	310	316	$^3F_3$	$_3\Gamma_2$	14 471	14 476		$_5\Gamma_2$	359	362	$^3F_3$	$_3\Gamma_2$	14 493	14 500
	$_5\Gamma_2$	460	463		$_0\Gamma_1$	14 488	14 486		$_5\Gamma_2$	—	507		$_0\Gamma_1$	14 511	14 523
	$_{-5}\Gamma_2$	—	470		$_3\Gamma_2$	14 503	14 503		$_4\Gamma_1$	513	510		$_1\Gamma_2$	14 529	14 531
	$_{-4}\Gamma_1$	474	474		$_2\Gamma_1$	14 537	14 535		$_5\Gamma_2$	522	534		$_3\Gamma_2$	14 561	14 575
	$_4\Gamma_1$	—	476		$_1\Gamma_2$	—	14 544		$_{-4}\Gamma_1$	530	533		$_2\Gamma_1$	14 564	14 570
					$_1\Gamma_2$	—	14 555						$_0\Gamma_1$	14 617	14 605
$^3F_4$	$_0\Gamma_1$	5650	5651		$_0\Gamma_1$	14 581	14581	$^3F_4$	$_4\Gamma_1$	5663	5678		$_1\Gamma_2$	14 625	14 597
	$_1\Gamma_2$	5695	5686						$_1\Gamma_2$	5711	5712				
	$_4\Gamma_1$	5705	5696	$^3F_2$	$_1\Gamma_2$	15 063	15 054		$_{-4}\Gamma_1$	5724	5702	$^3F_2$	$_1\Gamma_2$	15 078	15 071
	$_0\Gamma_1$	5735	5771		$_2\Gamma_1$	15 082	15 091		$_0\Gamma_1$	5768	5779		$_2\Gamma_1$	15 103	15 110
	$_1\Gamma_2$	5842	5844		$_2\Gamma_1$	15 102	15 103		$_1\Gamma_2$	5876	5864		$_2\Gamma_1$	15 123	15 124
	$_2\Gamma_1$	5922	5913		$_1\Gamma_2$	—	15 192		$_{-2}\Gamma_1$	5963	5955		$_1\Gamma_2$	—	15 222
	$_2\Gamma_1$	5940	5947		$_0\Gamma_1$	—	15 253		$_2\Gamma_1$	5976	5996		$_0\Gamma_1$	—	15 293
	$_3\Gamma_2$	5944	5929						$_3\Gamma_2$	5981	5970				
	$_3\Gamma_2$	5962	5954	$^1G_4$	$_0\Gamma_1$	21 088	21 102		$_3\Gamma_2$	6002	5991	$^1G_4$	$_0\Gamma_1$	21 092	21 107
					$_1\Gamma_2$	21 116	21 131						$_1\Gamma_2$	21 121	21 128
$^3H_{51}$	$_1\Gamma_2$	8228	8219		$_4\Gamma_1$	—	21 184	$^3H_5$	$_1\Gamma_2$	8230	8215		$_4\Gamma_1$	21 128	21 144
	$_0\Gamma_1$	8229	8216		$_0\Gamma_1$	21 324	21 309		$_0\Gamma_1$	8231	8216		$_0\Gamma_1$	—	21 287
	$_1\Gamma_2$	8347	8343		$_1\Gamma_2$	—	21 383		$_1\Gamma_2$	8369	8362		$_{-1}\Gamma_2$	—	21 357
	$_2\Gamma_1$	8354	8353		$_2\Gamma_1$	—	21 482		$_2\Gamma_1$	8379	8376		$_2\Gamma_1$	—	21 496
	$_5\Gamma_2$	8415	8403		$_3\Gamma_2$	21 498	21 503		$_5\Gamma_2$	8441	8426		$_3\Gamma_2$	21 535	21 523
	$_5\Gamma_2$	—	8441		$_2\Gamma_1$	21 569	21 554		$_{-5}\Gamma_2$	—	8479		$_2\Gamma_1$	21 613	21 588
	$_0\Gamma_1$	8465	8462		$_3\Gamma_2$	21 568	21 566		$_0\Gamma_1$	8500	8490		$_3\Gamma_2$	—	21 596
	$_3\Gamma_2$	—	8589						$_3\Gamma_2$	—	8624				
	$_4\Gamma_1$	8560	8591	$^3P_2$	$_2\Gamma_1$	27 747	27 766		$_4\Gamma_1$	8612	8630	$^3P_2$	$_2\Gamma_1$	27 743	27771
	$_4\Gamma_1$	8604	8609		$_2\Gamma_1$	27 810	27 811		$_4\Gamma_1$	8654	8662		$_{-2}\Gamma_1$	27 808	27 821
	$_3\Gamma_2$	8609	8609		$_1\Gamma_2$	—	27 826		$_3\Gamma_2$	8658	8660		$_1\Gamma_2$	—	27 835
					$_0\Gamma_1$	27 949	27 933						$_0\Gamma_1$	27 987	27 957
$^3H_{40}$	$_0\Gamma_1$	12 593	12 591		$_1\Gamma_2$	27 966	27 962	$^3H_4$	$_0\Gamma_1$	12 603	12 599		$_1\Gamma_2$	28 000	27 989
	$_1\Gamma_2$	12 596	12 604						$_1\Gamma_2$	12 606	12 605				

In the collected list of observed energy levels in table 3, some differences can be seen with regards to the energy levels presented in table 1 of [13] and in table 3 of [14]. Taking into account the preliminary simulation of the $4f^{12}$ configuration in KGdW, these differences correspond to either the removal of uncertain and low intense energy levels or to the revision of formerly indicated light polarizations under which they were observed.

The scheme of observed CF energy levels for Tm^{3+} in KLuW has been established in a parallel way to this of Tm^{3+} in KGdW, authorized by the likeliness shown by 6 K optical spectra of Tm^{3+} in both crystals. As expected, both sequences are very similar, with a few more energy levels detected in the low temperature Tm-KLuW OA and PL spectra (table 3).

The simulation adequately reproduces the experimental Tm^{3+} energy level sequences in both KGdW and KLuW crystals, with overall agreements σ = 13.0 and 15.7 cm^{-1}, respectively, see table 4. In no case were large individual discrepancies between experimental and calculated energy levels found (table 3). The final results are summarized in table 3 for the energy levels and in table 4 for adjusted FI and CF parameters.

4.3. Systematic variations in the phenomenological crystal field strength

The confidence in these phenomenological parameters and the physical meaning of the fits is supported not only by the low σ values obtained, but also by their smooth variation with regard to previous calculations performed for other configurations: $4f^2$ Pr^{3+} [30], $4f^3$ Nd^{3+} [42], $4f^{10}$ Ho^{3+} and the closest, $4f^{11}$ Er^{3+} [31] in the KGdW host.

Figure 4 shows the variation of phenomenological CF parameters as a function of the number of f electrons in

Table 4. Free-ion and C_2 crystal field parameters (cm^{-1}) for Tm^{3+} in $KRE(WO_4)_2$, RE = Gd^{3+} or Lu^{3+}, laser crystals. Italics indicate crystal field parameters calculated from SOM [32] (overlap between Tm^{3+} and ligand (oxygen) orbital wavefunctions $\rho = 0.06$, effective charge for oxygen $= -1$). Values in parentheses refer to estimated standard deviations in the indicated parameter. Values in square brackets were not varied in the fitting.

	Tm-$KG(WO_4)_2$		Tm-$KLu(WO_4)_2$	
E^0		17 575(1)		17 590(1)
E^1		6790(3)		6768(3)
E^2		33.76(2)		33.73(2)
E^3		668.7(2)		669.1(2)
α		17.54(5)		17.70(5)
β		[−720]		[−720]
γ		[1820]		[1820]
ζ		2634.1(8)		2632.0(9)
M^0 [a]		[3.0]		[3.0]
P^2 [b]		[700]		[700]
B_0^2	*447*	299(16)	*441*	332(17)
B_2^2	*276*	363(11)	*388*	412(11)
B_0^4	*−783*	−893(26)	*−905*	−976(31)
B_2^4	*269*	36(26)	*398*	78(28)
$i\,B_2^4$	*−736*	−676(19)	*−711*	−747(19)
B_4^4	*−170*	−36(28)	*−387*	−38(27)
$i\,B_4^4$	*247*	276(29)	*146*	354(33)
B_0^6	*−211*	−27(39)	*−97*	−31(41)
B_2^6	*205*	231(32)	*170*	104(32)
$i\,B_2^6$	*108*	48(30)	*63*	−8(30)
B_4^6	*79*	−139(28)	*−197*	−46(36)
$i\,B_4^6$	*24*	119(28)	*59*	62(29)
B_6^6	*−168*	−34(37)	*−30*	−159(33)
$i\,B_6^6$	*156*	176(28)	*185*	144(33)
S^{2c}	*265*	266	*315*	300
S^4	*474*	456	*526*	509
S^6	*144*	137	*133*	99
S^T	*325*	315	*362*	346
L		51		56
d_m		10.2		12.7
σ [d]		13.0		15.7
Residue		5430.4		9132.7

[a] M^0, M^2, M^4 were constrained by the ratios $M^2 = 0.56M^0$, $M^4 = 0.32M^0$.
[b] P^2, P^4, P^6 were constrained by the ratios $P^4 = 0.75P^2$, $P^6 = 0.50P^2$.
[c] Strength parameters calculated with expressions in [22].
[d] $\sigma = [\sum(\Delta_i)^2/(L-p)]^{1/2}$, $\Delta_i = E_o - E_c$, L number of levels, p number of parameters.

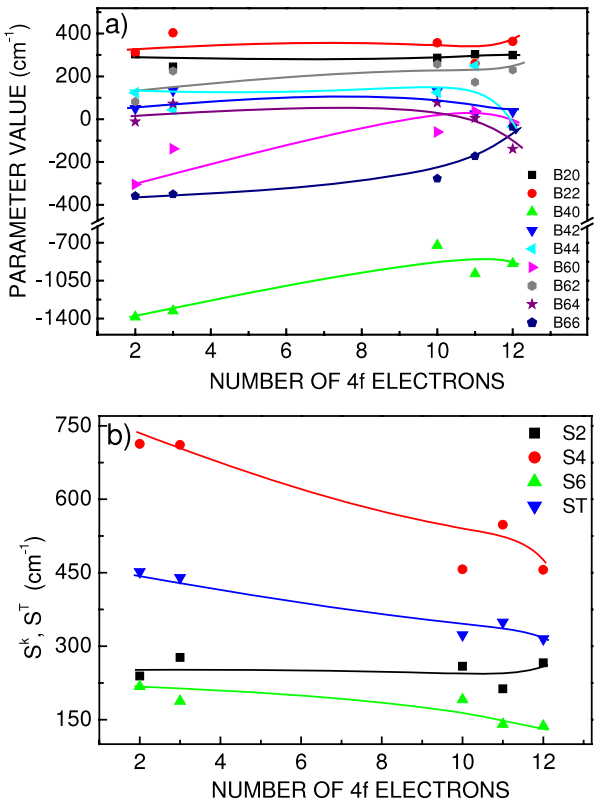

Figure 4. Variation of (a) phenomenological CF parameters and (b) CF strengths, for $4f^N$ configurations in RE-KGdW crystals. Set of data for $4f^2$ Pr^{3+}, $4f^{10}$ Ho^{3+}, $4f^{11}$ Er^{3+} and $4f^{12}$ Tm^{3+} are from the current authors [30, 31] and this work through the same model for free-ion and CF simulation. Data for $4f^3Nd^{3+}$ are from [42].

the KGdW series. The CF effect would be expected to weaken within this series when the nuclear charge to which the electrons are subjected increases from Pr^{3+} to Tm^{3+}, since the electron orbitals are pulled closer to the nucleus. But, apart from the nature of the optically active RE^{3+} center, the CF is obviously affected by the distances and bonding angles that characterize the crystallographic site of RE^{3+} in the host. If some reduction in unit cell parameters appears when the ionic radius of the optically active RE^{3+} impurity is getting smaller, and this supposes a parallel reduction in some RE^{3+}–O distance(s), or a broader distribution of distances around RE^{3+}, the short-range CF parameters (and the CF strength) would increase.

In fact, these CF parameters are especially sensitive to modifications in the close coordination shell of the active RE^{3+} ion. As shown in figure 4(a), an evolution to nearly constant magnitude can describe the behavior of short-range B_0^2 parameters from $4f^2$ to $4f^{12}$ configurations, while somewhat higher magnitudes can describe the same behavior in B_2^2 parameters. It seems that the CF weakening due to the nuclear charge increase criterion is compensated, and for B_2^2 even surpassed, by its enhancement derived of the reduction of some RE–O distance from Pr^{3+} to Tm^{3+}-doped crystals.

When, for a given crystalline host the number of CF parameters is large, the knowledge of the relative S^k ($k = 2, 4, 6$) and total S^T CF strength parameters is a useful tool for comparison of the CF interaction strength across the $4f^N$ series. S^2, S^4 and S^6 are rotational invariants of the CF (see the corresponding definitions in equation (4) [22]), which represent the short-, mid- and long-range CF strengths, respectively, in connection with the spatial expansion of CF effects. Given the high number of four- and six-rank parameters involved in the CF potential at the RE crystal site in the monoclinic KREW structure, trends in medium- and long-range CF effects must be summarized through corresponding S^4 and S^6 strengths. For the KGdW host, using results from

Table 5. Spectroscopic data of Tm-KRE$(WO_4)_2$, RE = Gd or Lu.

	Tm-KGdW	Tm-KLuW
$\sigma_{ABS}(\times 10^{-20}$ cm$^2)E \parallel N_m$	≈5.5(λ = 801 nm)	5.95 (λ = 802 nm)
$\sigma_{EMI}(\times 10^{-20}$ cm$^2)E \parallel N_m$ [a]	3.07 (λ = 1834 nm)	4.20 (λ = 1841 nm)
Lower laser level (cm^{-1})	474	530
Thermal population@300 K	2.68%	2.22%
Radiative lifetime $^3F_4$ (ms)	0.8	1.483 (J–O)
Fluorescence lifetime $^3F_4$ (ms)	1.76	1.34
Maximum phonon value (cm^{-1})	902	908
Reference	[8, 13]	[11]

[a] Recalculated values with the energy levels calculated by the current crystal field analysis.

the current as well as previous CF analyses [30, 31, 42], it is clear that S^4 and S^6 evolve with negative slopes from Pr^{3+} to Tm^{3+}. Also, the overall CF strength, S^T, which accounts for all CF parameters and describes the total CF strength, shows a clear decreasing trend along the series, although for Ho^{3+} some regain of the S^T magnitude is depicted. Discontinuities in the evolution of individual CF parameters along the RE-KGdW series, such as the observed inflection points in the general behavior, are similar to these observed in extensively studied RE-doped crystal hosts [15, 17, 20, 43].

Differences between the sets of CF parameters for Tm^{3+} in KGdW and KLuW crystals reflect specific crystallographic features of the C_2 sites they are occupying. Larger values of B_0^2 and B_2^2 parameters for KLuW suggest a more ionic and distorted Tm^{3+} short-range environment than in KGdW. This fact agrees with the larger distribution of Lu–O distances (2.217(7)–2.765(5) Å), along with the shorter average Lu–O distance ($\bar{d}_{Lu-O}$ = 2.385(8) Å) [24] in the coordination polyhedron LuO_8 compared to those in GdO_8 (2.271(12)–2.650(11) Å and $\bar{d}_{Gd-O}$ = 2.404(12) Å) [35]. Moreover, RE^{3+} local environments can also be numerically featured by the calculated distortion degree $\Delta_d \times 10^3$ of the corresponding REO_8 polyhedron [44]: 8.6 and 3.7 (note that the $\Delta_d \times 10^3$ distortion degree for the LuO_8 polyhedron has been corrected as two times those indicated in [24]), for RE = Lu and Gd, respectively. Higher absolute values of B_q^4 CF parameters and S^4 strengths for Tm-KLuW have the same origin. However, the trend is reversed for long-range B_q^6 and S^6 parameters, which are higher for Tm-KGdW. This can be explained by the more compact and covalent WO_6 octahedral arrangement around Tm^{3+} sites in KLuW [24] than in KGdW [35].

4.4. Room temperature Tm^{3+} spectroscopic properties in KREW (RE = Gd or Lu)

Table 5 contains the room temperature absorption cross sections σ_{ABS} associated with the infrared pumping ($^3H_6 \rightarrow {}^3H_4$) and emission ($^3F_4 \rightarrow {}^3H_6$) channels. The $^3F_4 \rightarrow {}^3H_6$ emission cross sections, σ_{EMI}, can be determined by using the reciprocity principle [45]

$$\sigma_{EMI}(E) = \sigma_{GSA}(E) \times (Z_l/Z_u) \times \exp\left[(E_{zl} - E)/k_B T\right] \quad (6)$$

where E_{zl} is the energy gap between the lowest Stark levels of the $^3F_4$ and $^3H_6$ multiplets, E is the light energy, Z_l and Z_u are the partition functions of the lower and upper multiplets, $Z_i = \sum_i \exp(-E/k_B T)$, where E_i is the energy position of the Tm^{3+} levels in these multiplets. It is clear that a poor knowledge of the Tm^{3+} energy level sequences could contribute to the uncertainty of σ_{EMI}. For instance, the Z_l/Z_u value previously used for Tm-KGdW seems underestimated, since it was based on a PL measurement that did not allow the correct identification either of the total splitting of the $^3H_6$ multiplet or the distribution of the corresponding Stark energy levels.

The Tm^{3+} laser at $\lambda \approx 1.9$ μm operates as a quasi-three-level laser system and therefore its efficiency depends strongly on the population of the ground state. Calculation of the gain cross section, $\sigma_{GAIN}(\lambda) = \beta\sigma_{EMI}(\lambda) - (1-\beta)\sigma_{GSA}(\lambda)$, where β represents the ratio of the Tm^{3+} ions in the excited state to the total ion density, which is a first estimation of the laser capability as well as the expected oscillation wavelength, further requires the accurate energy level sequences provided by the CF simulation in the studied crystals.

Using the experimentally determined energy levels of the Tm^{3+} $^3H_6$ state, the electronic thermal population in the upper Stark level of the terminal laser state $^3H_6$ is evaluated in both materials. The values are 2.68% and 2.22% for KGdW and KLuW, respectively. The larger $^3H_6$ splitting favors KLuW, inducing more favorable thermal populations of the involved energy levels, and thus lowering the laser threshold.

As shown in table 5, σ_{GSA} and σ_{EMI} are larger for KLuW than for KGdW. The intensity of the optical transition can be enhanced by the increased hybridization of the 4f orbitals in the lattice valence band for combined Lu^{3+} and Tm^{3+} doping [46], or via the 'intensity borrowing mechanism' introduced by Wybourne [47], in addition to the intermediate coupling scheme caused by spin–orbit interaction and to the J-mixing mechanisms originated from interactions via the crystal field potential. We suppose than the higher similarity of the Lu^{3+} and Tm^{3+}, from the electronic point of view, improves the hybridization of the 4f orbitals compared to Gd^{3+} and Tm^{3+}, favoring radiative transitions and leading to higher cross sections.

Finally, the lower lifetime of $^3F_4$ thulium in KLuW is also expected due to its higher CF strength.

5. Conclusions

With respect to crystal growth conditions KLuW is a more suitable host than KGdW for Tm^{3+} doping. The higher cooling

rates and lower temperature required to obtain macrodefect-free Tm-KLuW single crystals result in low economical cost for its growth. The Tm^{3+} energy levels in both KGdW and KLuW hosts have been determined using crystal field simulations in accordance with the C_2 symmetry of the occupied crystal site. Higher crystal field strength and correspondingly larger splitting for the $^3H_6$ Tm^{3+} ground state in KLuW result in lower threshold for laser oscillation. Furthermore, a borrowing mechanism that enhances the intensity of electronic transitions due to the higher electronic similarity among 4f orbitals of Lu^{3+} and Tm^{3+} compared to Gd^{3+} and Tm^{3+} could be at the origin of the higher absorption and emission cross sections observed for Tm^{3+} in the KLuW crystal.

Acknowledgments

We acknowledge financial support from the Spanish Government by the projects MAT2005-06354-C03-01/C03-02 and MAT2008-06729-C02-01/C02-02, and from the Catalan Government by the project 2005SGR658. The authors would like to thank the staff of Serveis Científico-Tècnics of the University of Barcelona (UB) for the EPMA measurements.

References

[1] Fried N M 2005 *Lasers Surg. Med.* **36** 52
[2] Li C, Song J, Shen D, Kim N S, Ueda K, Huo Y, He S and Cao Y 1999 *Opt. Express* **4** 12
[3] Mihalcea R M, Webber M E, Baer D S, Hanson R K, Feller G S and Chapman W B 1998 *Appl. Phys.* B **67** 283
[4] Han X, Cano-Torres J M, Rico M, Cascales C, Zaldo C, Mateos X, Rivier S, Griebner U and Petrov V 2008 *J. Appl. Phys.* **103** 083110
[5] Wu J, Jiang S, Luo T, Geng J, Peyhambarian N and Barnes N P 2006 *IEEE Photonics Technol. Lett.* **18** 334
[6] Honea E C, Beach R J, Sutton S B, Speth J A, Mitchell S C, Skidmore J A, Emanuel M A and Payne S A 1995 *IEEE J. Quantum Electron.* **33** 1592
[7] Saito H, Chodha S, Chang R S F and Djeu N 1992 *Opt. Lett.* **17** 189
[8] Petrov V, Güell F, Massons J, Gavalda J, Sole R M, Aguilo M, Diaz F and Griebner U 2004 *IEEE J. Quantum Electron.* **40** 1244
[9] Jani M G, Barnes N P, Murria K E, Hart D W, Quarles G J and Castillo V K 1997 *IEEE J. Quantum Electron.* **33** 112
[10] Aggarwal R L, Ripin D J, Ochoa J R and Fan T Y 2005 *J. Appl. Phys.* **98** 103514
[11] Mateos X, Petrov V, Liu J, Pujol M C, Griebner U, Aguiló M, Díaz F, Galan M and Viera G 2006 *IEEE J. Quantum Electron.* **42** 1008
[12] Petrov V, Pujol M C, Mateos X, Silvestre O, Rivier S, Aguiló M, Solé R M, Liu J, Griebner U and Díaz F 2007 *Laser Photon. Rev.* **1** 179
[13] Güell F, Mateos X, Gavaldá J, Solé R M, Aguiló M, Diaz F and Massons J 2004 *J. Lumin.* **106** 109
[14] Silvestre O, Pujol M C, Rico M, Güell F, Aguiló M and Díaz F 2007 *Appl. Phys.* B **87** 707
[15] Cascales C and Zaldo C 2006 *Chem. Mater.* **18** 3742
[16] Pujol M C, Solé R, Nikolov V, Gavaldà J, Massons J, Zaldo C, Aguiló M and Díaz F 1999 *J. Mater. Res.* **14** 3739
[17] Carnall W T, Goodman G L, Rajnak K and Rana R S 1989 *J. Chem. Phys.* **90** 3443
[18] Wybourne B G 1965 *Spectroscopic Properties of Rare Earths* (New York: Interscience)
[19] Porcher P 1989 *Fortran Routines REEL and IMAGE for Simulation of d^N and f^N Configurations Involving Real and Complex Crystal-Field Parameters* Paris unpublished
[20] Cascales C, Sáez-Puche R and Porcher P 1995 *J. Solid State Chem.* **114** 52
[21] Cascales C, Zaldo C, Caldiño U, García Solé J and Luo Z 2001 *J. Phys.: Condens. Matter* **13** 8071
[22] Chang N C, Gruber J B, Leavitt R P and Morrison C A 1982 *J. Chem. Phys.* **76** 3877
[23] Solé R, Nikolov V, Ruiz X, Gavaldà J, Solans X, Aguiló M and Diaz F 1996 *J. Cryst. Growth* **169** 600
[24] Pujol M C, Mateos X, Aznar A, Solans X, Suriñach S, Massons J, Díaz F and Aguiló M 2006 *J. Appl. Crystallogr.* **39** 230
[25] Aznar A, Silvestre O, Pujol M C, Aguiló M and Díaz F 2006 *Cryst. Growth Des.* **6** 1781
[26] Pujol M C, Aguiló M, Díaz F and Zaldo C 1999 *Opt. Mater.* **13** 33
[27] Koster G F, Dimmock J O, Wheeler R G and Statz H 1963 *Properties of the Thirty-Two Point Groups* (Cambridge, MA: MIT Press)
[28] Görller-Walrand C and Binnemans K 1996 Rationalization of crystal field parametrization *Handbook of the Physics and Chemistry of Rare Earths* vol 23, ed K A Gschneidner Jr and L Eyring (Amsterdam: Elsevier)
[29] Görller-Walrand C and Binnemans K 1998 Spectral intensities of f–f transitions *Handbook of the Physics and Chemistry of Rare Earths* vol 25, ed K A Gschneidner Jr and L Eyring (Amsterdam: Elsevier)
[30] Zaldo C, Rico M, Cascales C, Pujol M C, Massons J, Aguiló M, Díaz F and Porcher P 2000 *J. Phys.: Condens. Matter* **12** 8531
[31] Pujol M C, Cascales C, Rico M, Massons J, Díaz F, Porcher P and Zaldo C 2001 *J. Alloys Compounds* **323/324** 321
[32] Porcher P, Couto dos Santos M and Malta O 1999 *Phys. Chem. Chem. Phys.* **1** 397
[33] Cascales C, Sáez Puche R and Porcher P 1999 *Chem. Phys.* **240** 291
[34] Cascales C, Fernández J and Balda R 2005 *Opt. Express* **13** 2141
[35] Pujol M C, Solé R, Massons J, Gavaldà J, Solans X, Zaldo C, Díaz F and Aguiló M 2001 *J. Appl. Crystallogr.* **34** 1
[36] Gruber J B, Leavitt R P and Morrison C A 1981 *J. Chem. Phys.* **74** 2705
[37] Jayasankar C J, Reid M F and Richardson F S 1989 *Phys. Status Solidi* b **155** 559
[38] Holsa J, Lamminmaki R J, Antic-Fidancev E, Lemaitre-Blaise M and Porcher P 1995 *J. Phys.: Condens. Matter* **7** 5127
[39] Li Y, Yin M, Dong N, Makhov V N, Khaidukov N M and Krupa J C 2004 *J. Phys. Chem. Solids* **65** 1059
[40] Baraldi A, Capelletti R, Mazzera M, Riolo P, Amoretti G, Magnani N, Sani E, Toncelli A and Tonelli M 2005 *Phys. Status Solidi* c **1** 248
[41] Merkle L D, Gruber J B, Seltzer M D, Stevens S B and Allik T H 1992 *J. Appl. Phys.* **72** 4269
[42] Mironov V S and Li L E 1998 *J. Alloys Compounds* **279** 83
[43] Cascales C, Antic-Fidancev E and Lemaitre-Blaise Porcher P 1992 *J. Phys.: Condens. Matter* **4** 2721
[44] Shannon R D, Gummerman P S and Chenavas J 1975 *J. Am. Mineral.* **60** 714
[45] McCumber D E 1964 *Phys. Rev.* **136** A954
[46] Maunier C, Doualan J L, Moncorge R, Speghini A, Bettinelli M and Cavalli E 2002 *J. Opt. Soc. Am.* B **19** 1794
[47] Wybourne B G, Smentek L and Kedziorski A 2004 *Mol. Phys.* **102** 1105